Sarma, BB.; Plessow, PN.; Agostini, G.; Concepción Heydorn, P.; Pfänder, N.; Kang, L.; Wang, FR.... (2020). Metal-Specific Reactivity in Single-Atom Catalysts: CO Oxidation on 4d and 5d Transition Metals Atomically Dispersed on MgO. Journal of the American Chemical Society. 142(35):14890-14902. https://doi.org/10.1021/jacs.0c03627

Metal-specific reactivity in single-atom-catalysts: CO oxidation on 4d and 5d transition metals atomically dispersed on MgO

Bidyut B. Sarma[a], Philipp N. Plessow[b,*], Giovanni Agostini[c], Patricia Concepción[d], Norbert Pfänder[e], Liqun Kang[f], Feng R. Wang[f], Felix Studt[b], Gonzalo Prieto[a,d,*]

[a] Max-Planck-Institut für Kohlenforschung, Kaiser-Wilhelm-Platz 1, 45470 Mülheim an der Ruhr, Germany

[b] Institute of Catalysis Research and Technology, Karlsruhe Institute of Technology, Hermann-von-Helmholtz-Platz 1, D-76344 Eggenstein-Leopoldshafen, Germany

[c] ALBA Synchrotron Light Source, Carrer de la Llum 2-26, 08290, Cerdanyola del Vallès, Barcelona, Spain

[d] ITQ Instituto de Tecnología Química, Universitat Politècnica de València-Consejo Superior de Investigaciones Científicas (UPV-CSIC), Avenida de los Naranjos s/n, 46022 Valencia, Spain

[e] Max-Planck-Institut für chemische Energiekonversion, Stiftstraße, 45470 Mülheim an der Ruhr, Germany

[f] Department of Chemical Engineering, University College London, Torrington Place, London, WC1E 7JE, United Kingdom

Keywords: Single-atom catalysts; coordination confinement; XAS spectroscopy; In situ CO-FTIR; CO oxidation.

ABSTRACT: Understanding and tuning the catalytic properties of metals atomically dispersed on oxides are major stepping-stones towards a rational development of single-atom catalysts (SACs). Beyond individual showcase studies, the design and synthesis of structurally regular series of SACs opens the door to systematic experimental investigations of performance as a function of metal identity. Herein, a series of single-atom catalysts based on various 4d (Ru, Rh, Pd) and 5d (Ir, Pt) transition metals has been synthesized on a common MgO carrier. Complementary experimental (X-ray absorption spectroscopy) and theoretical (Density Functional Theory) studies reveal that, regardless of the metal identity, metal cations occupy preferably octahedral coordination MgO lattice positions under step-edges, hence highly confined by the oxide support. Upon exposure to O_2-lean CO oxidation conditions, FTIR spectroscopy indicates the partial de-confinement of the monoatomic metal centers driven by CO at pre-catalysis temperatures, followed by the development of surface carbonate species under steady-state conditions. These findings are supported by DFT calculations, which show the driving force and final structure for the surface metal protrusion to be metal-dependent, but point to an equivalent octahedral-coordinated M^{4+} carbonate species as the resting state in all cases. Experimentally, apparent reaction activation energies in the range of 96±19 kJ/mol are determined, with Pt leading to the lowest energy barrier. The results indicate that, for monoatomic sites in SACs, differences in CO oxidation reactivity enforceable via metal selection are of lower magnitude than those evidenced previously through the mechanistic involvement of adjacent redox centers on the oxide carrier, suggesting that tuning of the oxide surface chemistry is as relevant as the selection of the supported metal.

INTRODUCTION

Routes to disaggregate transition metal aggregates, i.e. nanoparticles and clusters, have been traditionally exploited to (re)disperse catalytically active metals on the surface of porous carriers, e.g. to regenerate supported catalysts which had undergone deactivation by metal sintering.[1-3] More recently, improvements in characterization methods, e.g. the advent of atomic-resolution aberration-corrected electron microscopy, have provided conclusive evidence that, under certain conditions, metals can be dispersed down to the atomic level, i.e. as isolated atoms, on oxide supports.[4-8] As a result, there is currently a blooming scientific interest in understanding, fine-tuning and exploiting the catalytic properties of so-called single-atom catalysts (SACs).[4,9-13]

Next to providing means for achieving a quantitative exposure of catalytically active metals to interaction with reactants, SACs hold the promise to successfully bridge the gap between the realms of homogeneous and heterogeneous catalysis by uniting technological advantages of the two disciplines.[14] On the one hand, the monoatomicity, (partial) positive charge and possibly uniform structure of active sites on SACs resemble features which are innate to metal centers in most molecular complexes operating as catalysts in solution. On the other hand, the solid nature and comparatively higher thermal and mechanical stability of SACs are essential for the technically uncomplicated catalyst handling, recovery and regeneration inherent to heterogeneous catalysis.

Over the last years, an ever-increasing number of studies address the catalytic performance of SACs in a large variety of reactions.[11,15-22] In certain instances, atomically dispersed metals have been revealed to underline unique reactivities previously ascribed to metal aggregates.[23] Beyond these valuable individual studies, and a limited number of head-to-head performance comparisons, this emerging research area would benefit from efforts to establish broader performance trends which would serve as a guideline for a more rational catalyst development. Screening the catalytic features of a series of structurally uniform materials, either computationally[24-25] or experimentally,[26-27] has proven instrumental in the past to establish valuable reactivity trends for various processes. Few recent studies have addressed

performance[28-29] and stability[30] trends in single-atom catalysts using *first principles* computational methods. Experimental studies pose, however, the challenge of designing, synthesizing and characterizing structurally regular series of catalysts at the atomic dispersion level.

Herein we investigate the catalytic properties of a series of 4d (Ru, Rh, Pd) and 5d (Ir, Pt) transition metals atomically dispersed on a common MgO carrier. MgO is a barely reducible support[31] with limited redox chemistry which is thus best suited to address the intrinsic redox catalytic properties of the supported metal atoms without support effects. Moreover, the relatively low energy of formation of surface topological defects, e.g. step-edges, on MgO provides a rough surface topology which is expected to be favorable for the establishment of ligand-type coordination and the stabilization of supported single metal atoms. The series of SACs was synthesized by oxidative dispersion of the corresponding metal oxides –obtained upon thermal decomposition of acetylacetonate precursors on a high-surface MgO carrier– at high temperature (1073 K). Metal dispersion was assessed by Scanning-Transmission Electron Microscopy (STEM), and the structure of the metals centers in the as-synthesized materials was studied by means of X-ray absorption spectroscopy (XAS), assisted by modeling using Density Functional Theory (DFT) calculations. The development of catalytically active sites was investigated by means of *in situ* Infrared (IR) spectroscopy, with input from DFT calculations.

Oxide-supported SACs have been studied as CO oxidation catalysts. While some previous studies underscore their high activity at low temperatures (<373 K),[32-33] other works report moderate performance and comparatively high reaction onset temperatures.[5,34-35] With this backdrop, it becomes highly relevant to elucidate whether these apparent discrepancies might root on prominent metal-specific phenomena. Herein, the series of structurally uniform MgO-supported SACs is exploited to systematically assess the role of metal identity on the CO oxidation catalytic performance.

EXPERIMENTAL

The series of M/MgO (M=Pt, Pd, Rh, Ru and Ir) catalysts were synthesized by depositing preset amounts of the corresponding metal acetylacetonate precursor onto a high-surface MgO support material by wet impregnation. The dried impregnate was then calcined at 1073 K in a muffle oven (stagnant air atmosphere) for 10 hours to induce metal oxide crystal disruption and dispersion. This re-dispersion temperature was selected on the bases of the so-called atom-trapping procedure developed by Datye and coworkers for Pt on CeO_2.[5-6]

X-ray powder patterns were collected on a Stoe STADI P transmission diffractometer equipped with a primary Ge (111) monochromator and a position sensitive detector using MoKα_1 radiation (λ= 0.7093 Å) after the samples were filled into glass capillaries (ø 0.5 mm). The dispersion and atomicity of metal species was investigated by means of high-angle annular dark-field scanning-transmission microscopy (HAADF-STEM) and X-ray absorption spectroscopy (XAS). HAADF-STEM experiments were performed using a C_s-probe corrected Hitachi HD-2700 dedicated Scanning-Transmission Electron microscope equipped with a cold field-emission gun and two EDAX Octane T Ultra W EDX detectors and operated at 200 kV. Prior to observation, finely ground powder samples were dry-cast on Cu grids coated with a holey carbon film. X-ray absorption spectra were recorded at the Rh K-edge (23.220 keV), Ru K-edge (22.117 keV), Pd K-edge (24.350 keV), Ir L_3-edge (11.215 keV), and Pt L_3-edge (11.564 keV), respectively, at the B18 beamline of the Diamond Light Source (UK), and the CLÆSS beamline (BL22) of the ALBA synchrotron light source (Spain). Measurements were performed either in transmission (after dilution of the sample with cellulose or boron nitride) or in fluorescence modes. EXAFS data analysis has been performed using the Demeter software package.[36] Data reduction and extraction of the χ(k) function has been performed using the Athena code (version 0.9.26). The experimental EXAFS spectra were analyzed starting from a series of DFT-optimized structural cluster models using FEFF6L via a data fitting analysis. A *k*-range up to 12 Å^{-1} with a Rbkg value of 1 were considered in the data reduction process. The following criteria for the free parameters were set to determine whether each model provided a physically sensible fit of the experimental data: (i) $0.6<S_0^2<1.1$, (ii) energy shift $|E_0|<11$ (eV), (iii) change in bond distance $|\Delta r| \leq 5\%$ $<R_{eff}>$ from the DFT-optimized model, and (iv) $0.001 < \sigma^2$.

The catalytic performance of the single-atom catalysts was evaluated for the oxidation of CO in stoichiometric O_2 excess. Tests were carried out in a packed-bed glass reactor (ID 50 mm) placed inside a vertically aligned oven. An amount of catalyst (200-300 µm sieved fraction) corresponding to 1 µmol metal was diluted with pure MgO (previously calcined at 1073 K) to achieve an overall bed length of 10 mm. Prior to reaction, the catalysts were pre-treated in flow of He (99.999, 30 mL min^{-1}) at 423 K. After cooling down to RT, a gas flow of a synthetic gas mixture (volumetric contents: 1%CO, 20%O_2, He balance) was established at a total gas space velocity of 1800 mL µmol(metal)$^{-1}$ h^{-1}. Then the bed temperature was increased to 623 K with a constant heating rate of 2 K min^{-1} while determining the outlet concentrations of CO and CO_2 online using a non-dispersive IR ABB EL3020 gas analyzer.

The development of active sites and reaction mechanism were investigated by means of DFT calculations and *in situ* Fourier-Transform infrared (FTIR) spectroscopy. DFT calculations were carried out with the PBE functional[37] with Grimme's D3 dispersion[38] correction using the PAW method as implemented in the VASP program package[39-40] (see the Supporting Information for full details, total energies and structures). Free energies were computed using the rigid-rotator and harmonic oscillator approximation at 573 K and a reference pressure of 1 bar. Transition states were located using the ARPESS method.[41] Spectroscopic investigations were carried out using CO as surface probe molecule. Self-supported catalysts were mounted into a stainless steel cell featuring KRS-5 windows. Samples were initially decarbonated. Catalyst surface topologies were studied at 110 K via stepwise CO dosing at increasing pressures in the sub-mbar range. In another set of experiments, samples were exposed to CO oxidation conditions in the cell, mimicking the reaction settings applied *ex situ* to assess the catalytic performance of the M/MgO SACs. Spectra were in all cases recorded with a Bruker Vertex 70 spectrometer using a DTGS detector and acquiring at 4 cm^{-1}

resolution. Further details on the experimental methods and the DFT calculations are provided in the Supporting Information.

RESULTS AND DISCUSSION

Synthesis of single-atom catalysts. The as-synthesized MgO support showed a B.E.T. specific surface area of 250 m^2 g^{-1} and a rod-like primary nanocrystal morphology (Figure S1). Annealing of the metal-free support at 1073 K led to a significant particle growth into mostly cubic-shaped MgO crystals accompanied by a drop in the surface area to 35 m^2 g^{-1}, indicating that the selected annealing temperature is sufficiently high to promote significant surface mobility and reorganization in MgO. On this support, two series of catalysts were synthesized with low surface-specific metal contents of 0.1±0.06 and 0.7±0.1 M_{at} nm^{-2}, respectively (see Experimental section). Following metal deposition, higher specific surface areas were obtained after annealing (45-60 m^2 g^{-1}) indicating a noticeable surface stabilization of the MgO by the supported metals. X-ray diffraction analysis showed no diffractions ascribable to metal species, suggesting the lack of long-range order (Figure S2).

High-resolution, bright-field TEM showed the surface of the MgO support in the as-synthesized catalysts to be highly stepped (Figure 1). To further assess metal dispersion the materials were studied with Spherical Aberration-corrected High-Angle Annular Dark-Field Scanning-Transmission Electron Microscopy (Cs-HAADF-STEM). Figure 1 shows also representative STEM micrographs for catalysts based on all the studied metals. In all cases, isolated metal atoms could be observed, uniformly dispersed on the MgO support, owing to the significantly higher Z contrast of the former. As expected, higher local metal densities were observed for materials synthesized with a metal content of 0.7 M_{at} nm^{-2}, compared to materials prepared with a ca. 7-fold lower overall metal content. However, no metal agglomerates could be identified in either case, clearly indicating the prevalence of isolated metal atoms at these contents. In contrast, the concomitant presence of atomically dispersed species with metal oxide clusters was confirmed for materials synthesized with higher metal contents, i.e. >1.5 M_{at} nm^{-2} for Pd/MgO and Ru/MgO catalysts and >2.5 M_{at} nm^{-2} for the remaining metals (Figure S3), indicating that at these higher metal contents, those binding sites involved in the stabilization of isolated metal cations on MgO become saturated and the metal loaded in surplus segregates into agglomerates.

Structural model for isolated metal centers. Complementing the direct, albeit local STEM observation, the atomicity and local coordination environment of the supported metals was studied with X-ray absorption spectroscopy. Figure 2 shows the corresponding EXAFS spectra for the series of catalysts with 0.7 M_{at} nm^{-2} metal content, along with those for the corresponding bulk metal and oxide reference materials. Irrespective of the identity of the supported metal, the spectra showed no evidences for *M*-*M* or *M*-O-*M* coordination, compatible with the absence of metallic or oxide agglomerates on the MgO surface. In order to further extract structural information from the EXAFS spectra, a series of structural models for the isolated metal atoms at various coordination positions on MgO were developed and structurally optimized using DFT calculations. The models comprise a large variety of binding sites, both at flat (001) and stepped (301) MgO surfaces (a full description of the structural models is given in the Supporting Information). The different site motifs can be organized as a function of the 1st-shell (*M*-*O*) and 2nd-shell (*M*-O-*Mg*) coordination numbers (CNs) for the metal atom, which jointly might be regarded as a measure of its degree of confinement by the MgO support. Figure 3 shows the series of models scrutinized for Ru/MgO and Pt/MgO catalysts, organized on a 2D map of degree of confinement. Similar maps for catalysts based on Rh, Pd and Ir are provided in the Supporting Information (Figures S4-S6). The simulated structural motifs span from low-confinement positions, e.g. at flat terraces or kinks, to high-confinement positions, e.g. lattice positions underneath MgO step-edges or sub-surface octahedrally coordinated M^{4+} cations stabilized by a neighbouring Mg vacancy, to full coordination for sub-surface M^{2+} cations isomorphically substituting Mg^{2+} centers in the MgO lattice (corresponding to 1st- and 2nd-shell CNs of 6 and 12, respectively).

The DFT-optimized structures were rescaled to match the experimental lattice constant of MgO and taken as models to fit the experimental EXAFS spectra, considering the two first coordination shells around the metal atoms (see experimental section for details on the fitting criteria and Tables S1 to S15 in the Supporting Information for the full fitting results). As shown in Figure 3, and the corresponding Figures S4-S6 in the SI, structural models corresponding to relatively high-confinement of the metal center (1st and 2nd-shell CNs ≥4 and ≥10, respectively) were those which provided a reasonable fit of the experimental spectra for all metals studied. These results are in contrast to previous reports on single-atom catalysts synthesized via the adsorption of monometallic complexes on oxides,[15,42] or impregnation of soluble precursors at lower surface contents followed by lower-temperature thermal treatments, which reported comparatively lower average coordination numbers for the isolated metal atoms. It is hence inferred that the high-temperature oxidative redispersion synthesis route applied herein, which promotes significant atomic mobility also for the oxide carrier, results in the supported metal atoms occupying lower-energy, higher-coordination positions.

Whereas the presence of (a fraction of) metal atoms in far subsurface positions cannot be excluded, the fact that the materials show catalytic activity already from very low metal contents, i.e. 0.1 M_{at} nm^{-2} (*vide infra*) suggests strongly that metal sites occupy near-surface coordination positions in the as-synthesized materials, hence more accessible to reactants. With the only exception of Rh, for which the best fitting model corresponded to a structure with slightly higher coordination confinement, a site model which considers the isolated metal atom to sit under a MgO step-edge, with an incomplete octahedral coordination shell, describes the experimental EXAFS spectra well. This structural model was compatible also with the EXAFS spectra recorded for the series of catalysts with an even lower metal content of 0.1 M_{at} nm^{-2}, as demonstrated by the direct comparison of the EXAFS data (Figure S7) and the fitting results included in the supporting Table S16, respectively.

Experimental study of catalytic activity. The catalytic properties of the series of M/MgO SACs were evaluated in the

oxidation of CO under excess O_2 in an isothermal plug-flow reactor. In order to ensure a higher structural homogeneity of the single-atom sites, and to reduce the chances for high local activity and thus temperature microgradients within the catalyst bed, the series of catalysts incorporating the lowest loading of 0.1 M_{at} nm^{-2} was selected for the reactivity study.

Figure 4 shows the CO conversion light-off curves as a function of the reaction temperature for experiments performed at a constant metal-specific gas space velocity of 1800 mL μmol(metal)$^{-1}$ h^{-1}. The T_{50} parameter (temperature for 50% CO conversion under the applied reaction settings) was in the range of 551-647 K. These values are significantly higher than those reported earlier for catalysts based on dimers,[35] sub-nm nanoclusters[44-45] or nanoparticles[46-47] of these metals deposited on oxide carriers, indicating that, generally, metallic species of higher nuclearity are more suitable for low-temperature CO oxidation applications. Light-off curves could be reproduced in consecutive reaction experiments following the first full run, attesting to the stability of the active sites on exposure to high reaction temperatures and CO conversion levels (Figure S8).

Light-off temperatures depend on the experimental conditions and, for reactions involving the development of the active centers *in situ*, under operating conditions (*vide infra*), it additionally depends on the kinetics and efficiency of these processes. The activation energy, determined after catalysis onset, offers a more reliable means to establish comparisons in terms of intrinsic activity. Analysis of the catalytic data via an Arrhenius formalism (Figure 4) showed the apparent activation energy (E_{app}) for the reaction to vary in the range of 77 kJ mol^{-1} for Pt_1/MgO to 115 kJ mol^{-1} for Ru_1/MgO catalysts. Intermediate E_{app} values of 90, 98 and 112 kJ mol^{-1} were determined for Rh_1/MgO, Ir_1/MgO and Pd_1/MgO catalysts, respectively. These E_{app} values are comparable to those reported previously for individual oxide-supported single-atom catalysts based on Rh or Pt.[34-35,48] Lower overall reaction energy barriers have been found in cases where the isolated metal atoms cooperate with redox-active centers developed on the oxide support in their direct vicinity.[29,32,48] Therefore our experimental results illustrate the expected limited involvement of the MgO support –which displays a high energy of formation of surface oxygen vacancies (>$8{\cdot}10^2$ kJ mol^{-1})[49]– in CO oxidation catalysis, as required to assess the intrinsic catalytic performance of the isolated metal centers.

Density Functional Theory investigation of active site structure and reaction mechanism. Insights into the structure of the active centers and the reaction mechanism on the M/MgO SACs were obtained by DFT calculations. The MgO(301) surface has been used as a computational model because it provides an extended 001-facet as well as a step-edge. For the substitution of transition metal atoms into Mg-positions, we have used the bulk chemical potential of MgO and the chemical potential of O_2 in the gas phase as a reference.

In the absence of CO and under oxidizing conditions, i.e. conditions representative of the as-synthesized catalysts prior to their exposure to reaction settings, the most stable state is generally one where the transition metal atoms displace Mg in surface or subsurface lattice positions. Substitution into the subsurface leads to octahedral coordination and for Pd and Pt, this is found to be favorable only in the oxidation state +4, where a d^6 electron configuration is reached. In agreement with these computational prediction, core-electron binding energies compatible with an oxidation state +4 were experimentally ascertained by X-ray Photoelectron Spectroscopy (XPS) for the series of M/MgO SACs (Figure S9). Relative to the bulk metals, these species are stable over a wide temperature range (see Figure CM4, Computational Methods section in the Supporting Information).

According to our DFT results, in the absence of carbon oxide adsorbates, the energetically most stable state for the isolated metal atoms on the MgO(301)-surface is in all cases the isomorphic substitution of the metal cation into the surface below the MgO step-edge, with an additional oxygen atom coordinated to the transition metal and the Mg atom at the step. Remarkably, when CO is introduced as a ligand, the most stable state is in all cases a transition metal atom in a Mg-position in the step-edge with a coordinated CO-ligand (Section 2 in the Supporting Information). Under these conditions, for Pd and Pt the most stable oxidation state is +2, and the adsorption geometry is a Pd/Pt atom in the Mg position with an additionally adsorbed CO. The coordination number is formally five, but the surface visibly distorts towards a square planar coordination geometry, as expected for a d^8-configuration (see section 2 in the SI). In this distortion, the transition metal atom moves away from the surface so that the distance to the underlying oxygen atom (2.7 Å) is significantly increased with respect to the other Pt-O distances (2.1 Å). For Rh, Ir, and Ru, the most stable state is still in oxidation state +4, with an additional oxygen atom coordinated to the transition metal atom in the same step-edge position as for Pd and Pt. Metal-specific phase diagrams were computed as a function of the CO and O_2 chemical potentials (for details see section 2 in the Supporting Information). These calculations predict that the formation of metal carbonyl complexes, in less confined positions at the MgO step-edges, becomes favorable under conditions representative for the catalytic tests (P_{CO}=1 mbar, P_{O2}=200 mbar, T=573 K) for all metals.

Overall, DFT calculations on the active site structure are in good agreement with our experimental observations. Transition metal atoms are predicted to be most stable in high-confinement octahedrally-coordinated lattice positions, likely associated to step-edges on the MgO surface. This motif is in fair agreement with the experimental EXAFS results (*vide supra*), and it can thus be considered to reliably represent a structurally uniform metal site for the entire series of catalysts in their as-synthesized condition, i.e. prior to exposure to reaction conditions. Calculations suggest, however, the possibility for a restructuring of this single-atom centers under catalysis-relevant operation conditions.

Having established a reasonable structure for the single-atom active sites, we next investigated the CO oxidation mechanism for the cases of Pt/MgO and Pd/MgO SACs. Experimentally, these metals showed reaction apparent activation energies in the low and high range-ends, respectively. The results for Pt are compiled in Figure 5. We have started the investigation from the most stable surface Pt^{II} carbonyl complex under reaction conditions (labeled 1a in Figure 5). Adsorption of a second CO molecule as a sixth ligand is not favorable, as expected for the d^8-configuration. The first necessary step is the activation of O_2, which eventually leads to the formation of free

CO_2 and an adsorbed oxygen-ligand. The formed complex (1d) is very reactive and readily reacts with either CO or CO_2. The reaction with a second CO molecule is barrier-less and leads to the formation of a stable carbonyl (1e), which, after a small barrier for oxidation, forms a second, adsorbed CO_2 (1f). The reaction with a CO_2 molecule leads to the formation of a transition metal carbonate (2a). Both reactions are expected to be fast, although carbonate-formation requires a small energetic barrier. It is not possible to predict the rate constants for CO vs. CO_2-adsorption with much certainty. However, formation of carbonate is clearly expected to happen at some point. Since the carbonate complex is very stable, we also studied pathways for its decomposition. The most favorable mechanism that we have found for a forward reaction consists of the reaction of the carbonate with a second CO molecule resulting in a κ^2-C,O-bound ligand that is maybe easiest described as a CO_2-dimer (2c). This structure can indeed decompose into two CO_2 molecules with a moderate barrier. Overall, a similar free energy diagram was also obtained in the case of a Pd-based SAC (Figure S10). Based on these findings, we expect that the identified surface metal carbonate is the resting state of the active site under operation.

Figure 5 shows a free energy diagram computed for Pt. The competitive adsorption of CO and CO_2 on complex 1d and the fact that there are two free energy barriers of about 170 kJ mol^{-1} makes an estimate of the reaction rate and preferred reaction pathway somewhat difficult to address. Importantly, these free energy barriers do not correspond to the apparent activation energies determined from the Arrhenius plot. For a direct comparison, we have derived apparent activation energies from the free energy diagram in Figure 5 based on a rate determining step analysis for these two highest barriers (see section 2 in the SI for the corresponding Arrhenius plots). An E_{app} = 83 kJ mol^{-1} is found assuming TS(1b-1c) to be rate limiting, whereas E_{app} = 101 kJ mol^{-1} under the assumption of TS(2a-2b) being rate-determining. The experimentally derived value (77 kJ mol^{-1}) is closer to the first of these simulated values. Comparatively similar reaction energy barriers were obtained for a Pd_1/MgO catalyst (Figure S10). Additionally, a Mars-van-Krevelen mechanism has been proposed for CO-oxidation on SACs, also for barely reducible supports such as Al_2O_3.[50] We have studied the possibility of a Mars-van-Krevelen mechanism for the situation of a subsurface Pt atom in oxidation state +4 in the second layer of a MgO(001) surface. A free energy barrier of 186 kJ mol^{-1} has been found for the oxidation of CO to CO_2 by reducing Pt from oxidation state +4 to +2 and creating an oxygen vacancy (Figure S11). The barrier is therefore slightly higher than that for the oxidation pathway on the metal active site model at the MgO step-edge.

Overall, apparent activation energies determined experimentally and computationally are comparable. Deviations are – in addition to the limited accuracy of DFT – likely due to the complicated kinetics of the mechanism shown in Figure 5. The branching of the mechanism into two pathways complicates the kinetics, especially since the relative rates for this branching, corresponding to the competitive adsorption of CO_2 or CO, are difficult to compute accurately. An additional uncertainty of our analysis is introduced by description of the O_2-molecule that is known to be problematic with DFT at the GGA level of theory.[51-52] It should be noted that the MgO(301) step is only one conceivable model for a highly confined surface site and other sites with similar confinement are also possible.[29,50,53] Nevertheless, given our analysis of apparent activation energies and the computed pathway shown in Figure 5, we conclude that the described model of a transition metal atom substituted into a Mg-position at a MgO step-edge is a realistic active site model of the SACs investigated.

***In situ* and *operando* spectroscopy investigation.** The structure and dynamics of the metal centers during exposure to catalysis was assessed by means of X-ray absorption near-edge structure (XANES) and Fourier-Transform infrared (FTIR) spectroscopies.

In situ XANES experiments confirmed that the absorption edge energy determined for the as-synthesized catalysts remained essentially unmodified on exposure to catalysis in all cases, proving that all metals remain in an oxidized state under catalysis conditions and hence ruling out their reductive agglomeration into metallic clusters under the applied O_2-lean reaction settings (Figures S12-S16 in the Supporting Information).

The surface topology of selected M/MgO catalysts in their as-synthesized state was studied with FTIR, using CO as surface probe at 110 K. This analysis revealed two major bands in the υ_{CO} region, peaking at ca. 2155-60 cm^{-1} and 2143-47 cm^{-1}, respectively, alongside a minor additional contribution at ca. 2035-40 cm^{-1} (Figure 6a, and Figure S17). These band positions correspond to a P_{CO}~1 mbar, as band shifts of up to 4 cm^{-1} were observed as a function of the CO partial pressure in the sub-mbar range, likely as a result of the establishment of dipolar coupling effects between neighboring CO molecules as the adsorbate surface coverage increased. These three bands were also observed for the plain MgO support (Figure S18) and hence correspond to a catalyst surface which resembles by and large that of magnesium oxide. The dominant band at 2155-60 cm^{-1} has been unambiguously ascribed to CO linearly adsorbed on regular (Mg^{2+}_{5c}) terrace Lewis sites, while the bands at 2143-47 cm^{-1} and 2035-40 cm^{-1} have been associated to CO adsorbed in a tilted configuration at step-edge sites (Mg^{2+}_{5c}/ Mg^{2+}_{4c}) on the basis of experiments on MgO single crystals and thin films as well as DFT calculations.[54-56] While the spectra for M/MgO catalysts and the metal-free MgO support are resemblant, slight shifts in the peaking frequencies at a given P_{CO}, as well as a noticeable higher relative intensity of low-frequency contributions for the metal catalysts suggest that the atomically dispersed metals add to the stabilization of a higher density of step-edge surface defects on the MgO carrier and modify to a certain extent the Lewis acid (electronic) character of the coordinatively unsaturated *(cus)* surface Mg^{2+} centers. However, no bands which could be unequivocally ascribed to M-CO carbonyl species could be observed, which suggests the limited accessibility of the $M^{\delta+}$ cations to CO in the as-synthesized catalysts, in line with the high degree of surface confinement predicted by DFT and experimentally ascertained by EXAFS.

Exposure to reaction conditions brought about a significant catalyst surface reconstruction. This is illustrated in Figure 6b for Ru/MgO. Under flow of the CO oxidation gas mixture, none of those bands corresponding to Mg^{2+}-CO carbonyls –detected at 110K– could be observed at T≥298 K due to the desorption

of CO from these Lewis centers already at sub-ambient temperatures. However, further increasing the temperature to 373 K led to the emergence of two new bands at 2198 and 2215 cm^{-1}, respectively. These bands appear in the spectral region for the CO stretching in (poly)carbonyls of transition metals in high oxidation states.[57] In this case (Figure 6b), band frequencies are in fair agreement with the υ_{CO} vibrations registered at 2190-2216 cm^{-1} for $Ru(CO)_6^{2+}$ cationic carbonyl complexes[58] and can thus be tentatively assigned to CO linearly bound to $Ru^{\delta+}$ centers. The bands likely reflect the development of new surface sites via the protrusion of metal centers on the catalyst surface. This is in agreement with the DFT calculations, which suggest CO as a driving force for an energetically favored extraction of the metal cations from the initial high-confinement positions to a lower coordination state on the surface of the MgO. On further increasing the temperature, both bands vanished completely before the temperature of incipient catalysis (473 K), suggesting that the associated surface carbonyl species do not persist during reaction.

At the reaction temperature selected for the *operando* FTIR study –corresponding to the T_{50} determined in the catalysis tests in each case– no bands were detected in the υ_{CO} region for any catalyst, suggesting that under steady reaction conditions the concentration of molecularly adsorbed CO is negligible. Instead, bands developed in the 1200-1800 cm^{-1} region, which can be ascribed to the υ_{COO} vibrations of surface carbonate species that form and accumulate on the catalyst surface in the course of the reaction as a result of charge transfer from the Lewis basic O^{2-} anions on the MgO surface and readsorbed CO_2 product.[59-60] Two major species might be discerned in this spectral region based on the co-evolution of doublet bands. A first intense doublet peaking at 1308 and 1648 cm^{-1}, and a second doublet characterized by signals at 1364 and 1579 cm^{-1}. The split bands can be assigned to the $\upsilon_{COO,as}$ and the $\upsilon_{COO,s}$ stretching vibrations of surface carbonate species. The magnitude of the band splitting ($\Delta\upsilon_3$= $\upsilon_{COO,s}$- $\upsilon_{COO,as}$) is known to depend on the configuration of the coordination of the carbonate species to the surface cation/s as well as the polarizing power of the latter Lewis center/s, which in turn determines the negative partial charge on the surface oxygen ligands.[59-60] For the two sets of bands under discussion $\Delta\upsilon_3$ takes values of 340 cm^{-1} and 215 cm^{-1}, respectively. The former has been previously observed for bidentate carbonates on MgO.[59] In the case of the latter doublet, the magnitude of the band splitting (<300 cm^{-1}) does not allow ruling out a monodentate configuration unequivocally. Nevertheless, monodentate carbonates on MgO have been shown to typically have $\Delta\upsilon_3$<150 cm^{-1}.[59,62] Therefore, it stands to reason to assign this doublet to bidentate carbonate species bound to surface cations of lower Lewis acidity. Remarkably, both species showed notably different reactivity towards oxygen upon removal of CO from the gas atmosphere at the reaction temperature. While the first set of bands remained essentially unaltered, the second doublet underwent a noticeable decrease in intensity during an O_2 treatment following reaction (Figure 6c). Hence, whilst the stability of the former points to a steady surface coverage as spectators, the dynamic character of the latter at the reaction temperature suggests that they might be involved in catalysis.

The surface restructuring upon exposure to catalysis led to permanent changes of the catalyst surface topology. This was plainly revealed by CO-FTIR, at cryogenic conditions (110 K), after catalyst exposure to reaction conditions in the IR cell (Figure 6d). In all cases, a new band peaking at ca. 2175 cm^{-1} emerged first at low CO doses, underwent a red-shift to 2171-2166 cm^{-1} on increasing the CO surface coverage, and dominated the spectra in the υ_{CO} region over those bands in the 2130-2160 cm^{-1} range which were already detected on the surface of the catalyst prior to catalysis. Previous surface science studies have identified the band at 2175 cm^{-1} particularly in highly defective MgO thin films and ascribed it to CO bonded to highly coordinatively unsaturated Mg^{2+} sites, i.e. of marked Lewis acidic character. Remarkably, a post-catalysis O_2 treatment at the reaction temperature eliminated completely this feature and restored a low-temperature CO-FTIR spectrum which resembles very closely that for the pristine catalyst (Figure 6e). This result suggests that the surface defects associated with the new post-reaction spectroscopic feature might be stabilized by labile carbonate species, and can thus be healed upon oxidative desorption/decomposition of the latter. The creation of this specific type of surface defect sites during catalysis was observed regardless of the nature of the supported metal (Figure 6a and 6f, and Figure S17), as well as for the metal-free MgO support (Figure S18), indicating that their emergence is associated with the occurrence of catalysis rather than with the presence of supported metal species.

Overall, the FTIR results indicate that the supported metals are not accessible to CO on the pristine catalysts. The active centers develop under the reactive atmosphere at pre-catalysis temperatures (373-473 K). Their formation likely involves a CO-mediated de-confinement of the isolated metal centers and it leads to a significant and permanent surface reconstruction characterized by the stabilization of highly unsaturated Mg^{2+} Lewis centers on the MgO surface. Under steady reaction conditions, no M-CO carbonyl species are detected by IR, which is suggestive of the fact that the activated metal centers remain blocked by other adsorbates, likely carbonate species. On the one hand, this experimental evidence is in accord with the mechanistic proposal put forth on the basis of DFT calculations, that the resting state of the active sites corresponds to a surface metal center binding a carbonate species. On the other hand, it precludes a direct proof for the surface exposure of the metal centers on the catalyst surface using CO as spectroscopy reporter under catalysis conditions. Nevertheless, evidence for this could be gained indirectly. Indeed, following exposure to reaction conditions, the removal of O_2 from the gas phase, thus hampering further complete catalytic cycles, enabled CO to compete for the metal centers and translated into the reductive agglomeration of the metal species into small metallic clusters (Figure S19). XPS results after *in situ* treatment in 1%CO/(He+N_2) at the reaction temperature indicate that the extent of reduction induced by this treatment is metal-dependent. In the case of Ru >90% contribution from Ru^0 (BE $Ru_{3d5/2}$=280.0 eV) is observed after the treatment, while in the case of Pt/MgO, the contribution of metallic Pt^0 amounted to 34% (BE $Pt_{4f7/2}$=70.8 eV) while the remaining metal showed a BE $Pt_{4f7/2}$=73.3 eV, compatible with Pt(II). This metal reduction and clustering led to a change in the CO oxidation reactivity, e.g. lowering T_{50} for Ru/MgO and Pt/MgO catalysts by 47 K and 59 K, respectively, evidencing that metallic clusters contribute higher CO oxidation reactivities compared to single-atom sites on MgO (Figure S20). Such reductive metal agglomeration was found not to reverse under O_2-lean CO

oxidation conditions, as revealed by the observation of a steady reactivity for consecutive light-off experiments (Figure S20) and the persistence of metal clusters on the MgO surface (Figure S21). Overall, our results illustrate that the metal centers become exposed onto the catalyst surface following a pre-reaction activation, and underline the importance of considering atomic-level *fluxionality* –in response to the chemical environment– to understand the structure and performance of single-atom catalysts.

CONCLUSIONS

Oxidative redispersion at high temperature (1073 K) enables the synthesis of atomically dispersed catalysts based on various 4d and 5d transition metals on a common MgO support at surface specific metal contents ≤ 0.7 M_{at} nm^{-2}. Analysis of the preferred coordination environment for the supported metal atoms via complementary experimental (EXAFS) and theoretical (DFT) studies reveals that M^{4+} cations occupy preferentially high-confinement octahedral coordination lattice positions associated to MgO surface step-edges regardless of the metal identity. This renders a series of structurally regular and atomically dispersed catalysts which enables a systematic evaluation of metal-specific performance in single-atom catalysis experimentally. DFT calculations predict a restructuring of the monoatomic metal centers upon exposure to CO oxidation conditions. While the magnitude of the driving force for this site restructuring is found to be metal dependent, it favors the protrusion of the metal atoms to lower confinement surface positions, leading to metal carbonyl complexes at MgO step-edges, for the entire series of metals studied. Despite the generality of this phenomenon, its redox implications and the structure of the preferred surface carbonyl is found to depend on the metal identity. In the case of group 10 metals (Pd and Pt) the process favors metal reduction to a +2 oxidation state, whereas for group 8-9 metals (Ru, Rh and Ir) the metal oxidation state remains +4. First principles analyses of the CO oxidation mechanism for Pt_1/MgO and Pd_1/MgO catalysts point to a metal carbonate complex at a MgO step-edge as the resting state of the monoatomic sites under reaction conditions. Both the CO-driven surface protrusion of the metal centers and their binding to carbonate adsorbates in their catalytic resting state are supported by experimental FTIR spectroscopy results, which bear out the absence of metal carbonyl species on the catalyst surface under *operando* conditions. For all metals studied, a M^{4+} surface carbonate complex, with octahedral coordination at MgO step-edges, is predicted to be the most stable metal species under CO oxidation conditions, suggesting an analogous active site structure under catalysis settings regardless of the metal identity. Experimental apparent activation energies are in the range of 96±19 kJ/mol for the entire series of metals, with Pt leading to the lowest overall energy barrier. Light-off temperatures and reaction energy barriers are significantly higher than those typical of metal aggregates of higher nuclearity, underscoring that isolated metal centers on non-reducible oxide carriers are generally not ideal catalysts for low-temperature CO oxidation. Moreover, the results indicate that, for these monoatomic sites, differences in CO oxidation reactivity as a function of the metal identity are smaller compared to those which have proved enforceable via the mechanistic engagement of adjacent redox centers on the oxide carrier, emphasizing the importance of adjusting the oxide surface chemistry, in addition to metal selection, for the development of single-atom oxidation catalysts.

ASSOCIATED CONTENT

Supporting Information. Further experimental details, computational details and additional results on the DFT calculations and Cartesian coordinates for optimized structures, Supporting Figures S1-S18, and Supporting Tables S1-S16. This material is available free of charge via the Internet at http://pubs.acs.org.

AUTHOR INFORMATION

Corresponding Authors

[*]Philipp N. Plessow: philipp.plessow@kit.edu
[*]Gonzalo Prieto: prieto@mpi-muelheim.mpg.de; prieto@itq.upv.es

Notes

The authors declare no competing financial interest.

ACKNOWLEDGMENTS

XAS experiments were performed at B18 beamline, Diamond Light Source, United Kingdom (proposals Nr. SP17377 and SP19072) and BL22 beamline, ALBA Light Source, Spain (experiment 2019023278). Beamline scientists D. Gianolio (Diamond) and L. Simonelli and C. Marini (ALBA) are acknowledged for their assistance with beamline setup during XAS experiments. Authors are grateful to M. García, E. Andrés, M.E. Martínez and I. López (ITQ) for assistance during the XAS experiments. J. Ternieden (MPI-KOFO) is acknowledged for the performance of XRD experiments. J.M. Salas (ITQ) is acknowledged for his experimental contribution to the CO-FTIR studies, and M.D. Soriano and A. Muñoz for the recording of XP spectra. P.N.P. and F.S. acknowledge support by the state of Baden- Württemberg through bwHPC (bwUnicluster and JUSTUS, RV bw17D01) and support from the Helmholtz Association is also gratefully acknowledged. This research received funding from the Alexander von Humboldt Foundation (postdoctoral grant to B.B.S.), the Max Planck Society and the Fonds der Chemischen Industry (FCI, Germany). The authors are grateful to Prof. Ferdi Schüth for the provision of lab facilities and support throughout the project. Funding from the Spanish Ministry of Science, Innovation and Universities (projects SEV 2016-0683 and RTI2018-096399-A-100) is also acknowledged.

REFERENCES

1. Ruckenstein, E.; Hu, X. D., Mechanism of redispersion of supported metal catalysts in oxidative atmospheres. *Langmuir* **1985,** *1* (6), 756-760.
2. Szymura, J. A., Studies on Redispersion and Stability of Platinum in Pt/MgO System during Oxygen Treatment at High Temperatures. *Zeitschr. Anorg. u. Allg. Chemie.* **1986,** *542* (11), 232-240.
3. Morgan, K.; Goguet, A.; Hardacre, C., Metal Redispersion Strategies for Recycling of Supported Metal Catalysts: A Perspective. *ACS Catal.* **2015,** *5* (6), 3430-3445.
4. Qiao, B.; Wang, A.; Yang, X.; Allard, L. F.; Jiang, Z.; Cui, Y.; Liu, J.; Li, J.; Zhang, T., Single-atom Catalysis of CO Oxidation Using Pt_1/FeO_x. *Nat. Chem.* **2011,** *3* (8), 634-641.

5. Jones, J.; Xiong, H.; DeLaRiva, A. T.; Peterson, E. J.; Pham, H.; Challa, S. R.; Qi, G.; Oh, S.; Wiebenga, M. H.; Pereira Hernández, X. I.; Wang, Y.; Datye, A. K., Thermally Stable Single-Atom Platinum-on-Ceria Catalysts via Atom Trapping. *Science* **2016,** *353* (6295), 150-154.
6. Kunwar, D.; Zhou, S.; DeLaRiva, A.; Peterson, E. J.; Xiong, H.; Pereira-Hernández, X. I.; Purdy, S. C.; ter Veen, R.; Brongersma, H. H.; Miller, J. T.; Hashiguchi, H.; Kovarik, L.; Lin, S.; Guo, H.; Wang, Y.; Datye, A. K., Stabilizing High Metal Loadings of Thermally Stable Platinum Single Atoms on an Industrial Catalyst Support. *ACS Catal.* **2019,** *9* (5), 3978-3990.
7. Liu, L.; Zakharov, D.N.; Arenal R.; Concepcion, P.; Stach, E.A.; Corma, A. Evolution and stabilization of subnanometric metal species in confined space by in situ TEM. *Nat. Commun.* **2018***, 9*, 574.
8. Sarma, B. B.; Kim, J.; Amsler, J.; Agostini, G.; Weidenthaler, C.; Pfänder, N.; Arenal, R.; Concepción, P.; Plessow, P.; Studt, F.; Prieto, G., One-Pot Cooperation of Single-Atom Rh and Ru Solid Catalysts for a Selective Tandem Olefin Isomerization-Hydrosilylation Process. *Angew. Chem. Int. Ed.* **2020***, 59,* 5806-5815.
9. Yang, X.-F.; Wang, A.; Qiao, B.; Li, J.; Liu, J.; Zhang, T., Single-Atom Catalysts: A New Frontier in Heterogeneous Catalysis. *Acc. Chem. Res.* **2013,** *46* (8), 1740-1748.
10. Gates, B. C.; Flytzani-Stephanopoulos, M.; Dixon, D. A.; Katz, A., Atomically dispersed supported metal catalysts: perspectives and suggestions for future research. *Catal. Sci. Technol.* **2017,** *7* (19), 4259-4275.
11. Wang, A.; Li, J.; Zhang, T., Heterogeneous single-atom catalysis. *Nat. Rev. Chem.* **2018,** *2* (6), 65-81.
12. Babucci, M.; Fang, C.-Y.; Perez-Aguilar, J. E.; Hoffman, A. S.; Boubnov, A.; Guan, E.; Bare, S. R.; Gates, B. C.; Uzun, A., Controlling catalytic activity and selectivity for partial hydrogenation by tuning the environment around active sites in iridium complexes bonded to supports. *Chem. Sci.* **2019,** *10* (9), 2623-2632.
13. Amsler, J.; Sarma, B. B.; Agostini, G.; Prieto, G.; Plessow, P. N.; Studt, F., Prospects of Heterogeneous Hydroformylation with Supported Single Atom Catalysts. *J. Am. Chem. Soc.* **2020,** *142* (11), 5087-5096.
14. Cui, X.; Li, W.; Ryabchuk, P.; Junge, K.; Beller, M., Bridging homogeneous and heterogeneous catalysis by heterogeneous single-metal-site catalysts. *Nat. Catal.* **2018,** *1* (6), 385-397.
15. Uzun, A.; Ortalan, V.; Browning, N. D.; Gates, B. C., A site-isolated mononuclear iridium complex catalyst supported on MgO: Characterization by spectroscopy and aberration-corrected scanning transmission electron microscopy. *J. Catal.* **2010,** *269* (2), 318-328.
16. Lang, R.; Li, T.; Matsumura, D.; Miao, S.; Ren, Y.; Cui, Y.-T.; Tan, Y.; Qiao, B.; Li, L.; Wang, A.; Wang, X.; Zhang, T., Hydroformylation of Olefins by a Rhodium Single-Atom Catalyst with Activity Comparable to RhCl(PPh3)3. *Angew. Chem. Int. Ed.* **2016,** *55* (52), 16054-16058.
17. Chen, Y.; Ji, S.; Sun, W.; Chen, W.; Dong, J.; Wen, J.; Zhang, J.; Li, Z.; Zheng, L.; Chen, C.; Peng, Q.; Wang, D.; Li, Y., Discovering Partially Charged Single-Atom Pt for Enhanced Anti-Markovnikov Alkene Hydrosilylation. *J. Am. Chem. Soc.* **2018,** *140* (24), 7407-7410.
18. Zhang, X.; Sun, Z.; Wang, B.; Tang, Y.; Nguyen, L.; Li, Y.; Tao, F. F., C–C Coupling on Single-Atom-Based Heterogeneous Catalyst. *J. Am. Chem. Soc.* **2018,** *140* (3), 954-962.
19. Chen, Z.; Vorobyeva, E.; Mitchell, S.; Fako, E.; Ortuño, M. A.; López, N.; Collins, S. M.; Midgley, P. A.; Richard, S.; Vilé, G.; Pérez-Ramírez, J., A heterogeneous single-atom palladium catalyst surpassing homogeneous systems for Suzuki coupling. *Nat. Nanotechnol.* **2018,** *13* (8), 702-707.
20. Millet, M.-M.; Algara-Siller, G.; Wrabetz, S.; Mazheika, A.; Girgsdies, F.; Teschner, D.; Seitz, F.; Tarasov, A.; Levchenko, S. V.; Schlögl, R.; Frei, E., Ni Single Atom Catalysts for CO_2 Activation. *J. Am. Chem. Soc.* **2019,** *141* (6), 2451-2461.
21. Li, J.; Guan, Q.; Wu, H.; Liu, W.; Lin, Y.; Sun, Z.; Ye, X.; Zheng, X.; Pan, H.; Zhu, J.; Chen, S.; Zhang, W.; Wei, S.; Lu, J., Highly Active and Stable Metal Single-Atom Catalysts Achieved by Strong Electronic Metal–Support Interactions. *J. Am. Chem. Soc.* **2019,** *141* (37), 14515-14519.
22. Tang, Y.; Wei, Y.; Wang, Z.; Zhang, S.; Li, Y.; Nguyen, L.; Li, Y.; Zhou, Y.; Shen, W.; Tao, F. F.; Hu, P., Synergy of Single-Atom Ni_1 and Ru_1 Sites on CeO_2 for Dry Reforming of CH_4. *J. Am. Chem. Soc.* **2019,** *141* (18), 7283-7293.
23. Malta, G.; Kondrat, S. A.; Freakley, S. J.; Davies, C. J.; Lu, L.; Dawson, S.; Thetford, A.; Gibson, E. K.; Morgan, D. J.; Jones, W.; Wells, P. P.; Johnston, P.; Catlow, C. R. A.; Kiely, C. J.; Hutchings, G. J., Identification of single-site gold catalysis in acetylene hydrochlorination. *Science* **2017,** *355* (6332), 1399-1403.
24. Falsig, H.; Hvolbæk, B.; Kristensen, I. S.; Jiang, T.; Bligaard, T.; Christensen, C. H.; Nørskov, J. K., Trends in the Catalytic CO Oxidation Activity of Nanoparticles. *Angew. Chem. Int. Ed.* **2008,** *47* (26), 4835-4839.
25. Latimer, A. A.; Kulkarni, A. R.; Aljama, H.; Montoya, J. H.; Yoo, J. S.; Tsai, C.; Abild-Pedersen, F.; Studt, F.; Nørskov, J. K., Understanding trends in C–H bond activation in heterogeneous catalysis. *Nat. Mater.* **2016,** *16*, 225.
26. Hensen, E. J. M.; Brans, H. J. A.; Lardinois, G. M. H. J.; de Beer, V. H. J.; van Veen, J. A. R.; van Santen, R. A., Periodic Trends in Hydrotreating Catalysis: Thiophene Hydrodesulfurization over Carbon-Supported 4d Transition Metal Sulfides. *J. Catal.* **2000,** *192* (1), 98-107.
27. Thornburg, N. E.; Thompson, A. B.; Notestein, J. M., Periodic Trends in Highly Dispersed Groups IV and V Supported Metal Oxide Catalysts for Alkene Epoxidation with H_2O_2. *ACS Catal.* **2015,** *5* (9), 5077-5088.
28. Yang, T.; Fukuda, R.; Hosokawa, S.; Tanaka, T.; Sakaki, S.; Ehara, M., A Theoretical Investigation on CO Oxidation by Single-Atom Catalysts M_1/γ-Al_2O_3 (M=Pd, Fe, Co, and Ni). *ChemCatChem* **2017,** *9* (7), 1222-1229.
29. Kropp, T.; Lu, Z.; Li, Z.; Chin, Y.-H. C.; Mavrikakis, M., Anionic Single-Atom Catalysts for CO Oxidation: Support-Independent Activity at Low Temperatures. *ACS Catal.* **2019,** *9* (2), 1595-1604.
30. O'Connor, N. J.; Jonayat, A. S. M.; Janik, M. J.; Senftle, T. P., Interaction trends between single metal atoms and oxide supports identified with density functional theory and statistical learning. *Nat. Catal.* **2018,** *1* (7), 531-539.

31. Tanaka, I.; Oba, F.; Tatsumi, K.; Kunisu, M.; Nakano, M.; Adachi, H., Theoretical Formation Energy of Oxygen-Vacancies in Oxides. *Mater. Trans.* **2002,** *43* (7), 1426-1429.
32. Therrien, A. J.; Hensley, A. J. R.; Marcinkowski, M. D.; Zhang, R.; Lucci, F. R.; Coughlin, B.; Schilling, A. C.; McEwen, J.-S.; Sykes, E. C. H., An atomic-scale view of single-site Pt catalysis for low-temperature CO oxidation. *Nat. Catal.* **2018,** *1* (3), 192-198.
33. Lu, Y.; Wang, J.; Yu, L.; Kovarik, L.; Zhang, X.; Hoffman, A. S.; Gallo, A.; Bare, S. R.; Sokaras, D.; Kroll, T.; Dagle, V.; Xin, H.; Karim, A. M., Identification of the active complex for CO oxidation over single-atom Ir-on-$MgAl_2O_4$ catalysts. *Nat. Catal.* **2019,** *2* (2), 149-156.
34. Zhang, B.; Asakura, H.; Yan, N., Atomically Dispersed Rhodium on Self-Assembled Phosphotungstic Acid: Structural Features and Catalytic CO Oxidation Properties. *Ind. Eng. Chem. Res.* **2017,** *56* (13), 3578-3587.
35. Wang, H.; Liu, J.-X.; Allard, L. F.; Lee, S.; Liu, J.; Li, H.; Wang, J.; Wang, J.; Oh, S. H.; Li, W.; Flytzani-Stephanopoulos, M.; Shen, M.; Goldsmith, B. R.; Yang, M., Surpassing the single-atom catalytic activity limit through paired Pt-O-Pt ensemble built from isolated Pt_1 atoms. *Nat. Commun.* **2019,** *10* (1), 3808.
36. Ravel, B.; Newville, M., ATHENA, ARTEMIS, HEPHAESTUS: data analysis for X-ray absorption spectroscopy using IFEFFIT. *J. Synch. Rad.* **2005,** *12* (4), 537-541.
37. Perdew, J. P.; Burke, K.; Ernzerhof, M., Generalized Gradient Approximation Made Simple. *Phys. Rev. Lett.* **1997,** *78* (7), 1396-1396.
38. Grimme, S.; Antony, J.; Ehrlich, S.; Krieg, H., A consistent and accurate ab initio parametrization of density functional dispersion correction (DFT-D) for the 94 elements H-Pu. *J. Chem. Phys.* **2010,** *132* (15), 154104.
39. Kresse, G.; Furthmüller, J., Efficient iterative schemes for ab initio total-energy calculations using a plane-wave basis set. *Phys. Rev. B* **1996,** *54* (16), 11169-11186.
40. Kresse, G.; Joubert, D., From ultrasoft pseudopotentials to the projector augmented-wave method. *Phys. Rev. B* **1999,** *59* (3), 1758-1775.
41. Plessow, P. N., Efficient Transition State Optimization of Periodic Structures through Automated Relaxed Potential Energy Surface Scans. *J. Chem. Theor. Comp.* **2018,** *14* (2), 981-990.
42. Hoffman, A. S.; Debefve, L. M.; Zhang, S.; Perez-Aguilar, J. E.; Conley, E. T.; Justl, K. R.; Arslan, I.; Dixon, D. A.; Gates, B. C., Beating Heterogeneity of Single-Site Catalysts: MgO-Supported Iridium Complexes. *ACS Catal.* **2018,** *8* (4), 3489-3498.
43. Ren, Y.; Tang, Y.; Zhang, L.; Liu, X.; Li, L.; Miao, S.; Sheng Su, D.; Wang, A.; Li, J.; Zhang, T., Unraveling the coordination structure-performance relationship in Pt_1/Fe_2O_3 single-atom catalyst. *Nat. Commun.* **2019,** *10* (1), 4500.
44. Gatla, S.; Aubert, D.; Agostini, G.; Mathon, O.; Pascarelli, S.; Lunkenbein, T.; Willinger, M. G.; Kaper, H., Room-Temperature CO Oxidation Catalyst: Low-Temperature Metal–Support Interaction between Platinum Nanoparticles and Nanosized Ceria. *ACS Catal.* **2016,** *6* (9), 6151-6155.
45. Guan, H.; Lin, J.; Qiao, B.; Yang, X.; Li, L.; Miao, S.; Liu, J.; Wang, A.; Wang, X.; Zhang, T., Catalytically Active Rh Sub-Nanoclusters on TiO_2 for CO Oxidation at Cryogenic Temperatures. *Angew. Chem. Int. Ed.* **2016,** *55* (8), 2820-2824.
46. Gaudet, J. R.; de la Riva, A.; Peterson, E. J.; Bolin, T.; Datye, A. K., Improved Low-Temperature CO Oxidation Performance of Pd Supported on La-Stabilized Alumina. *ACS Catal.* **2013,** *3* (5), 846-855.
47. Gänzler, A. M.; Casapu, M.; Doronkin, D. E.; Maurer, F.; Lott, P.; Glatzel, P.; Votsmeier, M.; Deutschmann, O.; Grunwaldt, J.-D., Unravelling the Different Reaction Pathways for Low Temperature CO Oxidation on Pt/CeO_2 and Pt/Al_2O_3 by Spatially Resolved Structure–Activity Correlations. *J. Phys. Chem. Lett.* **2019,** *10* (24), 7698-7705.
48. Nie, L.; Mei, D.; Xiong, H.; Peng, B.; Ren, Z.; Hernandez, X. I. P.; DeLaRiva, A.; Wang, M.; Engelhard, M. H.; Kovarik, L.; Datye, A. K.; Wang, Y., Activation of surface lattice oxygen in single-atom Pt/CeO_2 for low-temperature CO oxidation. *Science* **2017,** *358* (6369), 1419-1423.
49. Carrasco, J.; Lopez, N.; Illas, F.; Freund, H.-J., Bulk and surface oxygen vacancy formation and diffusion in single crystals, ultrathin films, and metal grown oxide structures. *J. Chem. Phys.* **2006,** *125* (7), 074711.
50. Kropp, T.; Mavrikakis, M., Brønsted–Evans–Polanyi relation for CO oxidation on metal oxides following the Mars–van Krevelen mechanism. *J. Catal.* **2019**, *377*, 577-581.
51. Wang, L.; Maxisch, T.; Ceder, G., Oxidation energies of transition metal oxides within the GGA+U framework. *Phys. Rev. B* **2006,** *73* (19), 195107.
52. Martínez, J. I.; Hansen, H. A.; Rossmeisl, J.; Nørskov, J. K., Formation energies of rutile metal dioxides using density functional theory. *Phys. Rev. B* **2009,** *79* (4), 045120.
53. Yang, T.; Fukuda, R.; Hosokawa, S.: Tanaka, T.; Sakaki, S.; Ehara, M., A Theoretical Investigation on CO Oxidation by Single-Atom Catalysts M_1/γ-Al_2O_3 (M=Pd, Fe, Co, and Ni). *ChemCatChem* **2017** , *9* , 1222-1229.
54. Soave, R.; Pacchioni, G., New bonding mode of CO on stepped MgO surfaces from density functional cluster model calculations. *Chem. Phys. Lett.* **2000,** *320* (3), 345-351.
55. Sterrer, M.; Risse, T.; Freund, H.-J., CO adsorption on the surface of MgO(001) thin films. *Appl. Catal. A: Gen.* **2006,** *307* (1), 58-61.
56. Trionfetti, C.; Babich, I. V.; Seshan, K.; Lefferts, L., Presence of Lithium Ions in MgO Lattice: Surface Characterization by Infrared Spectroscopy and Reactivity towards Oxidative Conversion of Propane. *Langmuir* **2008,** *24* (15), 8220-8228.
57. Mihaylov, M. Y.; Fierro-Gonzalez, J. C.; Knözinger, H.; Gates, B. C.; Hadjiivanov, K. I., Formation of Nonclassical Carbonyls of Au^{3+} in Zeolite NaY: Characterization by Infrared Spectroscopy. *J. Phys. Chem. B* **2006,** *110* (15), 7695-7701.
58. Wang, C.; Bley, B.; Balzer-Jöllenbeck, G.; Lewis, A. R.; Siu, S. C.; Willner, H.; Aubke, F., New homoleptic metal carbonyl cations: the syntheses, vibrational and ^{13}C MAS NMR spectra of hexacarbonyl-ruthenium(II) and-osmium(II) undecafluorodiantimonate(V),

$[Ru(CO)_6][Sb_2F_{11}]_2$ and $[Os(CO)_6][Sb_2F_{11}]_2$. *J. Chem. Soc. Chem. Commun.* **1995,** (20), 2071-2072.
59. Yasuo, F.; Kozo, T., Infrared Study of Carbon Dioxide Adsorbed on Magnesium and Calcium Oxides. *Bull. Chem. Soc. Japan* **1973,** *46* (6), 1616-1619.
60. Philipp, R.; Fujimoto, K., FTIR spectroscopic study of carbon dioxide adsorption/desorption on magnesia/calcium oxide catalysts. *J. Phys. Chem.* **1992,** *96* (22), 9035-9038.
61. Busca, G.; Lorenzelli, V., Infrared spectroscopic identification of species arising from reactive adsorption of carbon oxides on metal oxide surfaces. *Mater. Chem.* **1982,** *7* (1), 89-126.
62. Cornu, D.; Guesmi, H.; Krafft, J.-M.; Lauron-Pernot, H., Lewis Acido-Basic Interactions between CO_2 and MgO Surface: DFT and DRIFT Approaches. *J. Phys. Chem. C* **2012**, *116 (11)*, 6645-6654.

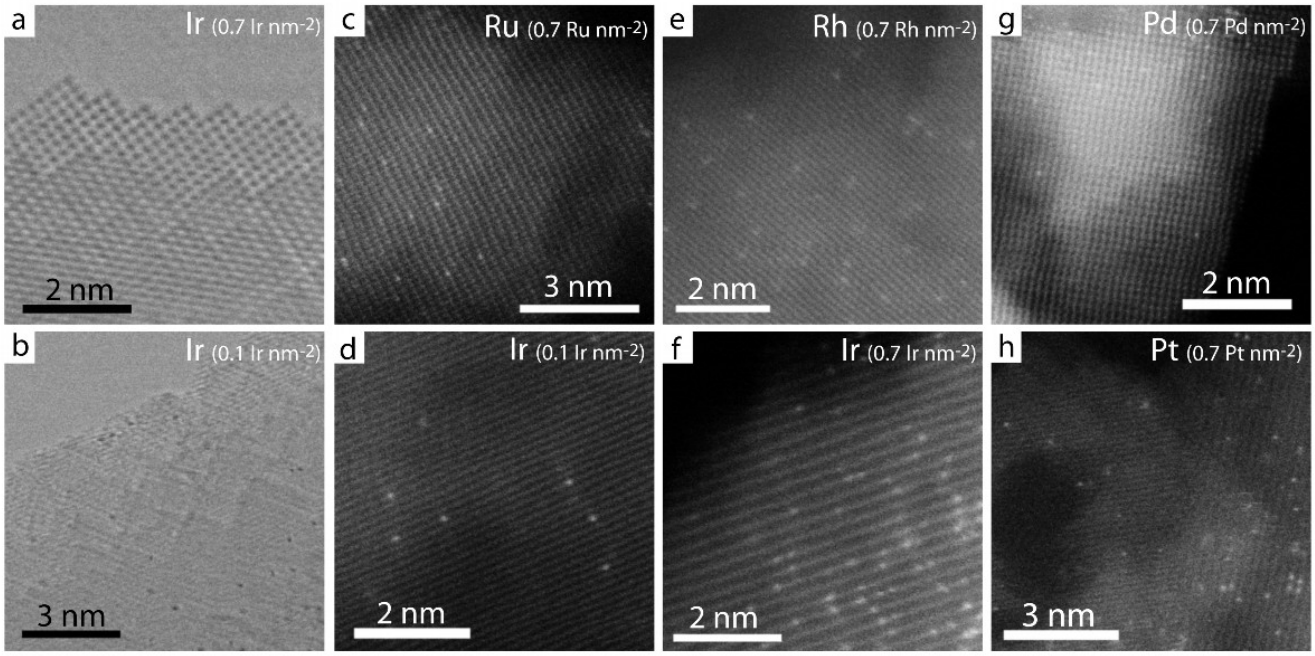

Figure 1: Bright-field STEM (a-b) and HAADF-STEM (c-h) micrographs for M/MgO atomically dispersed catalysts (M=Ru, Rh, Pd, Ir, Pt) synthesized with surface-specific metal contents of 0.1 and 0.7 M_{at} nm^{-2}, as indicated on the micrographs.

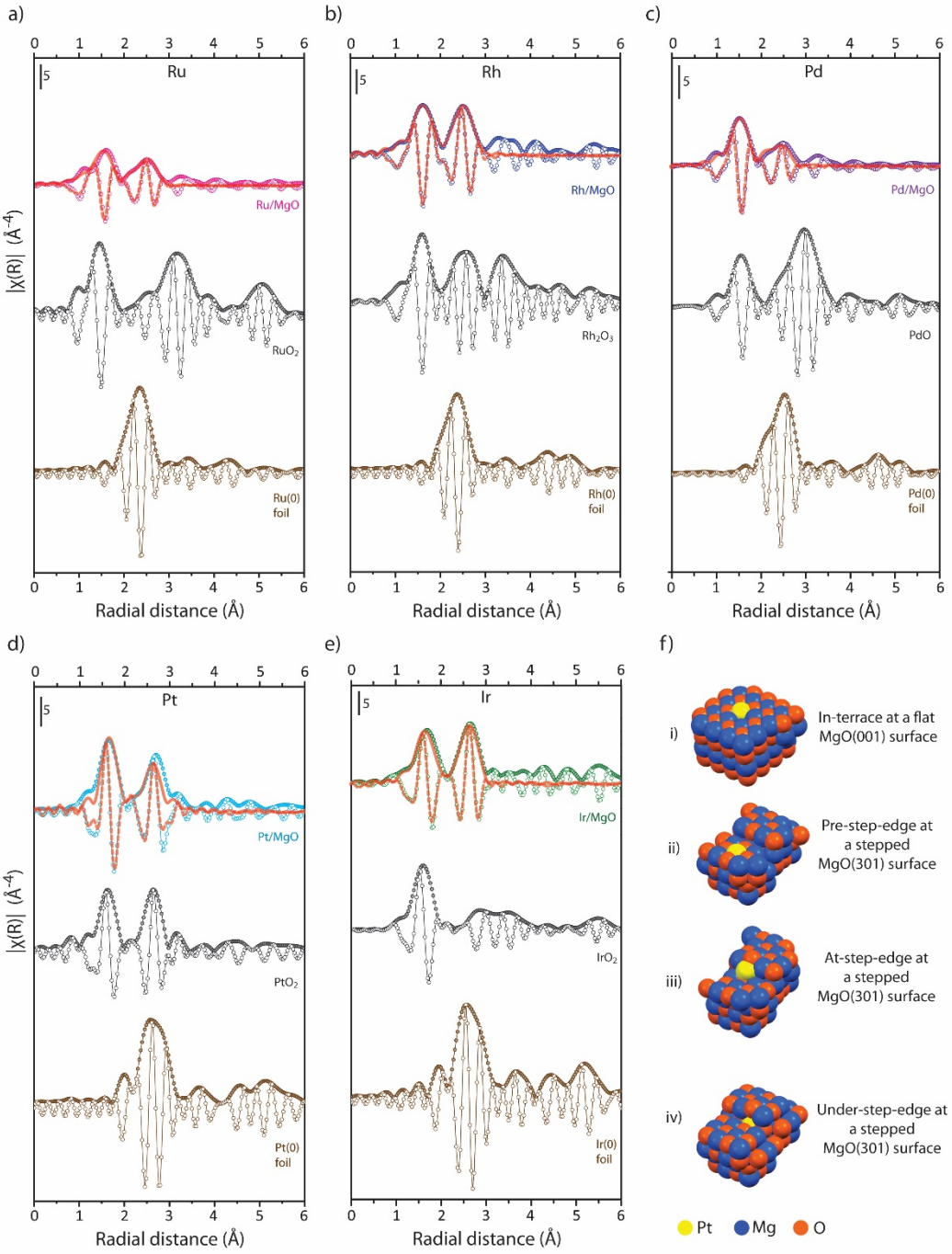

Figure 2: X-ray absorption spectroscopy characterization of atomically dispersed M/MgO catalysts. a-e) k^3-weighted EXAFS spectra in R-space for the series of M/MgO catalysts synthesized with a metal content of 0.7±0.1 M_{at} nm^{-2}.The corresponding spectra for bulk oxides and metal foils reference materials are also included in the plot. Scatter traces correspond to experimental data (closed symbols: real components; open symbols: imaginary components). Full lines correspond to the fits of the experimental data to the structural model corresponding to single metal atoms sitting under a MgO step-edge for Ru, Pd, Pt and Ir (structure iv in panel f). For Rh/MgO, the best-fitting single-atom site model corresponds to a structure with slightly higher metal coordination numbers (see Supporting Information). f) Selected DFT-optimized structural models for a single Pt atom on MgO, representative of those screened to fit the experimental EXAFS spectra: i) In-terrace at a flat MgO(001) surface, and ii) pre-step-edge, iii) at-step-edge and iv) under-step-edge at a stepped MgO(301) surface. Color codes: Blue (Mg), red (O), yellow (Pt).

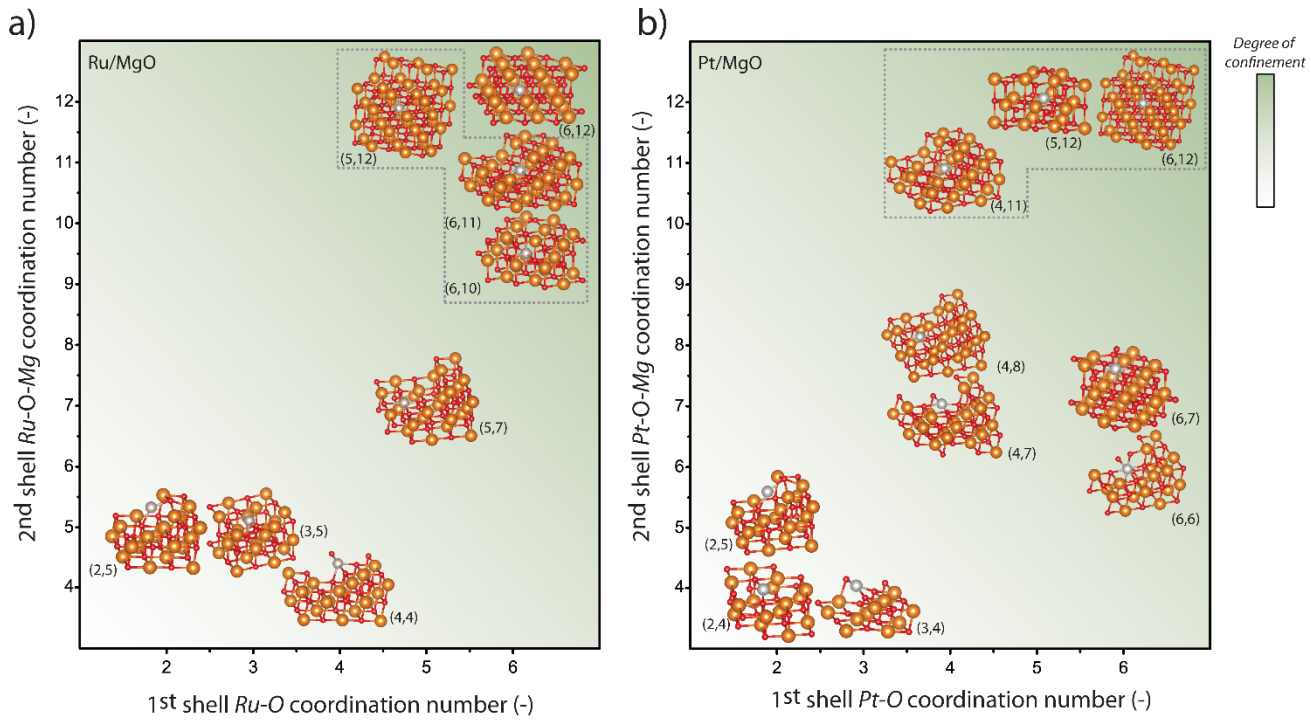

Figure 3: 2D plots showing various DFT-derived structural models for MgO-supported a) ruthenium and b) platinum single-atoms as a function of the 1st-shell *M-O* and 2nd-shell *M*-O-*Mg* coordination numbers for the metal atom. The background shade is a qualitative contour plot for the degree of confinement of the supported metal atom by the MgO support. The dashed line encloses site models which have been found to be compatible with the experimental EXAFS spectra for atomically dispersed catalysts with a 0.7 $M_{at}\,nm^{-2}$ metal content. Color code in model structures: orange (Mg), red (O), gray (supported metal). The labels included on the plots next to each structural model indicate the corresponding 1st- and 2nd-shell coordination numbers for the central metal atom. Similar maps for Rh/MgO, Pd/MgO and Ir/MgO are given as Supporting Figures S4, S5 and S6, respectively, in the Supporting Information.

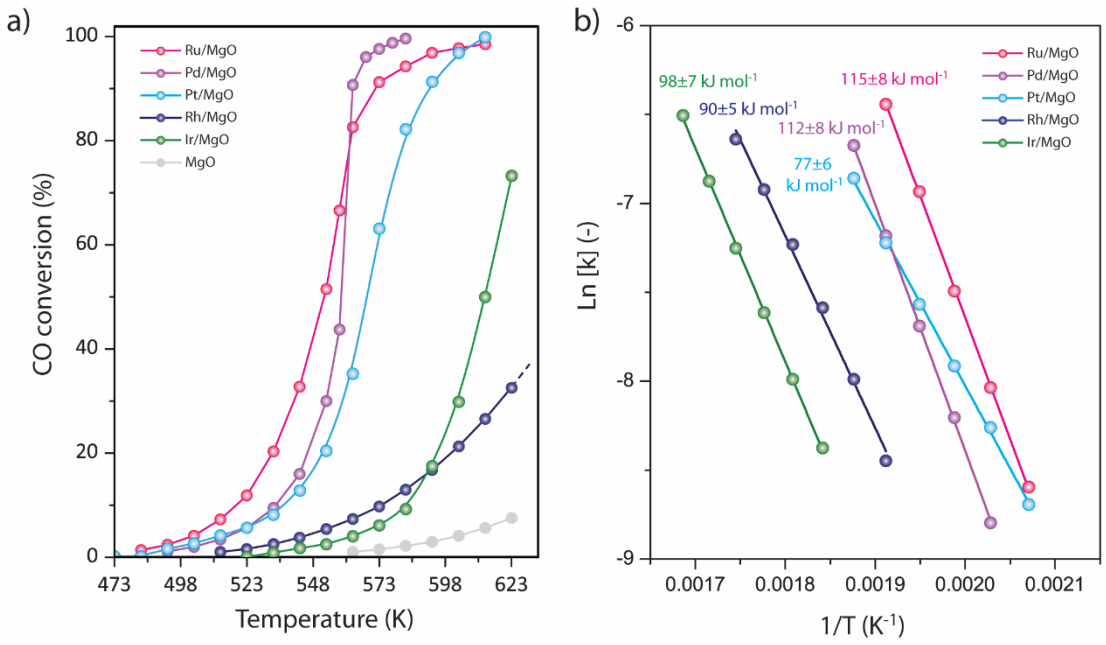

Figure 4: a) Evolution of CO conversion with the reaction temperature and b) Arrhenius plot derived from the pseudo-zero order kinetic rate constants and catalytic data at X_{CO}<10% for the series of atomically dispersed M/MgO catalysts with a 0.1 M_{at} nm^{-2} metal content. Uncertainties in the E_{app} values were derived from the analysis of two consecutive light-off experiments. Reaction conditions: P= 1 bar, gas feed composition (1%CO, 20%O_2, He balance), 1800 mL µmol(metal)$^{-1}$ h^{-1}, M=Ru, Rh, Pd, Ir or Pt.

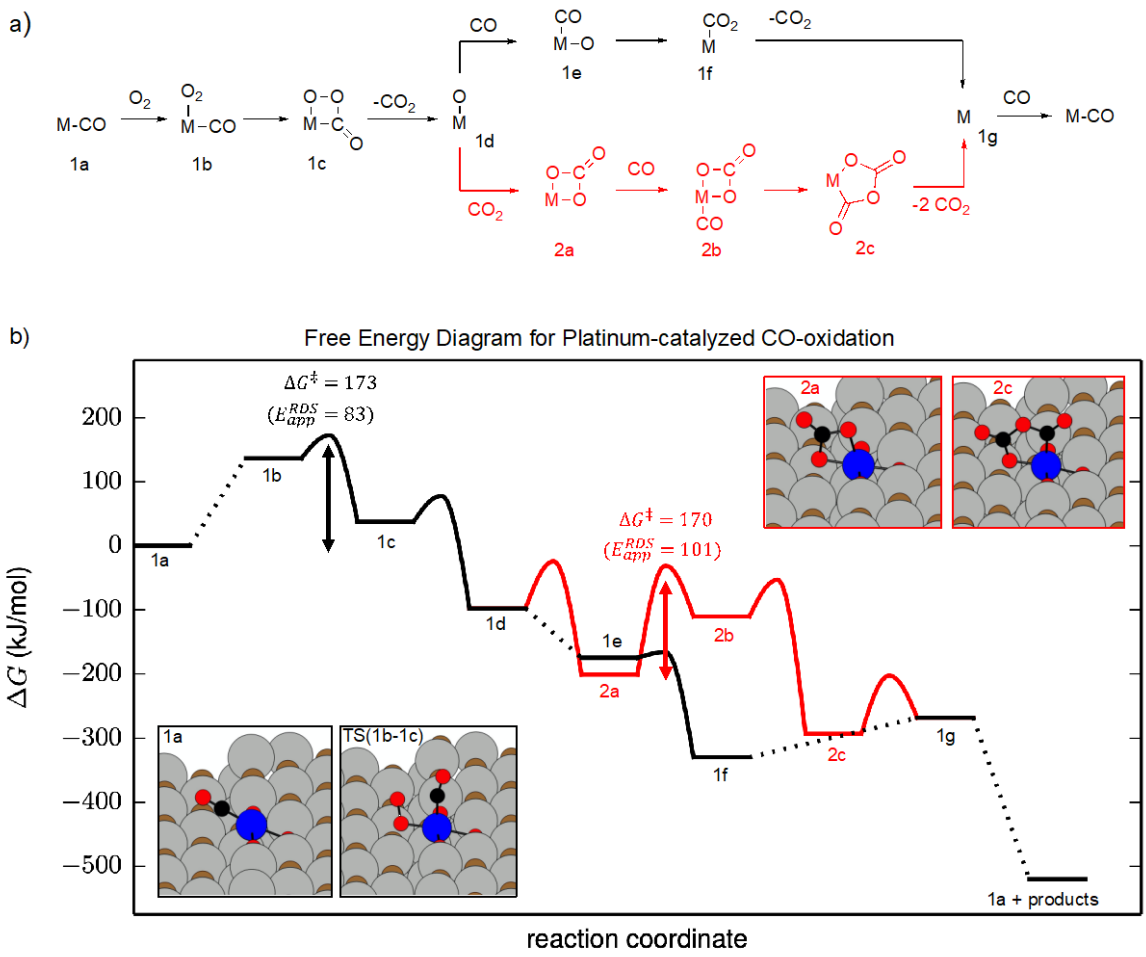

Figure 5: Mechanism investigated with DFT-calculations for Pt. a) Scheme for CO-oxidation mechanism starting from the metal carbonyl. b) Free energy diagram computed for Pt at 573 K and 1 bar reference pressure for the mechanisms shown in a) using the same labels. The two highest barriers are indicated and the values given in kJ/mol. Additionally, apparent activation energies as derived from these barriers and the rate-determining step (RDS) approximation are provided (see section 2 in the Supporting Information for the corresponding Arrhenius plots). Insets depict the atomic structures of important intermediates and transition states (color code: Mg: gray, lattice-O: brown, O: red, C: black, Pt: blue).

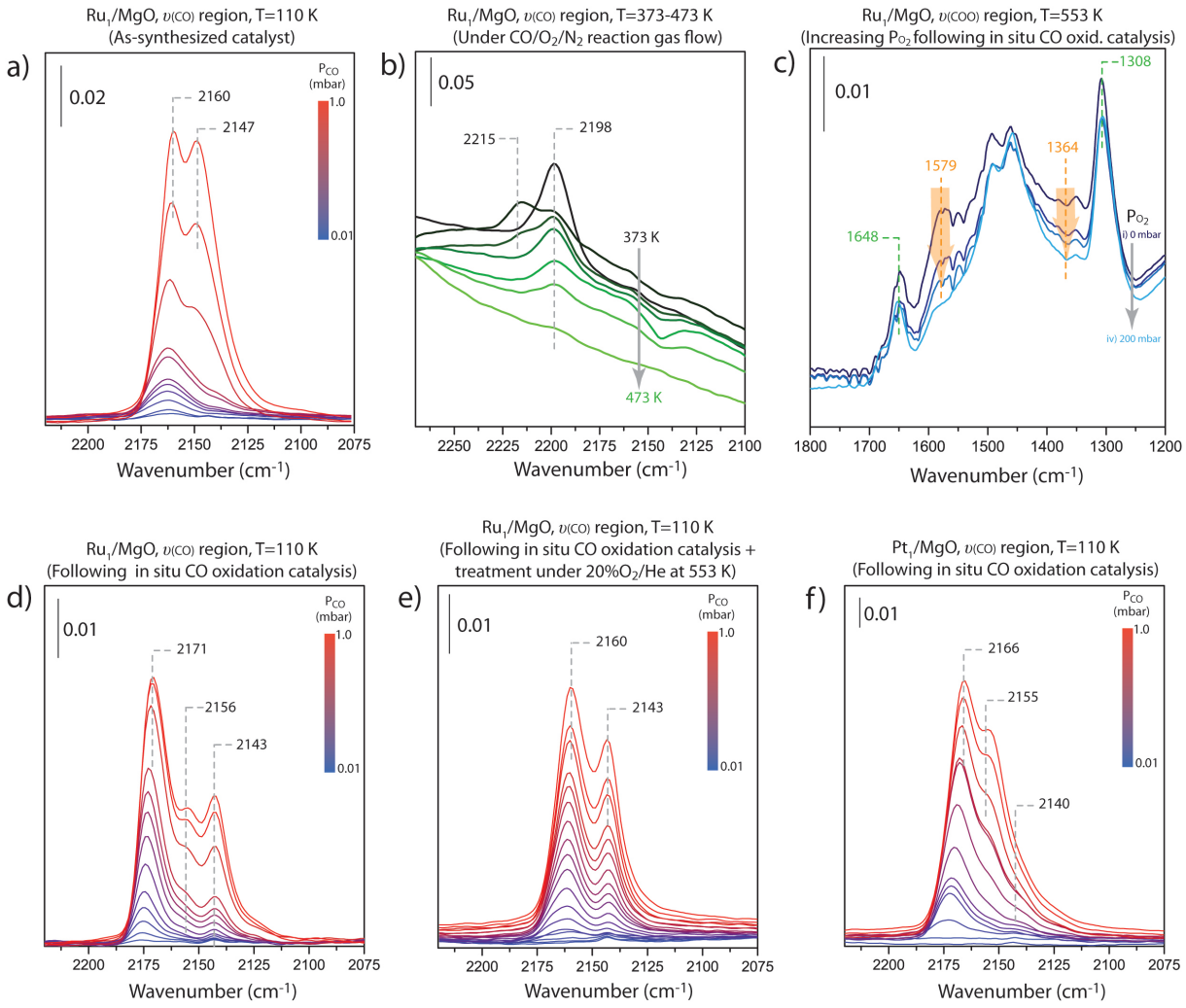

Figure 6: *In situ* and *operando* CO-FTIR spectroscopy. a) Spectra in the υ_{CO} region after increasing CO dosages on the surface of the as-synthesized Ru_1/MgO catalyst at 110 K. b) Temperature-resolved spectra in the υ_{CO} region for Ru_1/MgO exposed to flow of the reaction $CO/O_2/N_2$ mixture at increasing temperatures in the 373-473 K range. c) Spectra in the υ_{COO} region for Ru_1/MgO after exposure to CO oxidation reaction conditions (553 K), followed by cell evacuation and isothermal treatment under increasing O_2 partial pressures at the reaction temperature. d) Spectra in the υ_{CO} region after stepwise increasing CO dosages at 110 K on the surface of Ru_1/MgO after exposure to CO oxidation reaction conditions (553 K). e) Spectra in the υ_{CO} region after increasing CO dosages on the surface of Ru_1/MgO at 110 K after exposure to CO oxidation reaction conditions (553 K) followed by a treatment under $20\%O_2/N_2$ at the reaction temperature. f) Spectra in the υ_{CO} region after stepwise increasing CO dosages at 110 K on the surface of Pt_1/MgO after exposure to CO oxidation reaction conditions (553 K). Data corresponds in all cases to single-atom catalysts with a metal loading of 0.7 $M_{at}\,nm^{-2}$.

TABLE OF CONTENTS GRAPHIC